Modelling of the Peltier effect in magnetic multilayers

Isaac Juarez-Acosta, Miguel A. Olivares-Robles, Subrojati Bosu, Yuya Sakuraba, Takahide Kubota, Saburo Takahashi, Koki Takanashi, and Gerrit E. W. Bauer

Citation: Journal of Applied Physics **119**, 073906 (2016); doi: 10.1063/1.4942163
View online: http://dx.doi.org/10.1063/1.4942163
View Table of Contents: http://scitation.aip.org/content/aip/journal/jap/119/7?ver=pdfcov
Published by the AIP Publishing

Modelling of the Peltier effect in magnetic multilayers

Isaac Juarez-Acosta,[1] Miguel A. Olivares-Robles,[2] Subrojati Bosu,[3,4] Yuya Sakuraba,[4] Takahide Kubota,[3] Saburo Takahashi,[3] Koki Takanashi,[3] and Gerrit E. W. Bauer[3,5,6]
[1]*SEPI ENCB, Instituto Politecnico Nacional, Mexico D.F. 11340, Mexico*
[2]*SEPI ESIME-Culhuacan, Instituto Politecnico Nacional, Mexico D.F. 04430, Mexico*
[3]*Institute for Materials Research, Tohoku University, Sendai 980-8577, Japan*
[4]*National Institute for Materials Science, Ibaraki 305-0047, Japan*
[5]*WPI-AIMR, Tohoku University, Sendai 980-8577, Japan*
[6]*Kavli Institute of Nanoscience, Delft University of Technology, Lorentzweg 1, 2628 CJ Delft, The Netherlands*

(Received 26 October 2015; accepted 4 February 2016; published online 19 February 2016)

We model the charge, spin, and heat currents in ferromagnetic metal|normal metal|normal metal trilayer structures in the two current model, taking into account bulk and interface thermoelectric properties as well as Joule heating. The results include the temperature distribution as well as resistance-current curves that reproduce the observed shifted parabolic characteristics. Thin tunneling barriers can enhance the apparent Peltier cooling. The model agrees with the experimental results for wide multilayer pillars, but the giant effects observed for diameters $\lesssim$100 nm are still under discussion. © *2016 AIP Publishing LLC*. [http://dx.doi.org/10.1063/1.4942163]

I. INTRODUCTION

Thermoelectric effects result from the coupling between energy and particle transport in conductors. An example is the heat current that is associated with a charge current and proportional to a material parameter called Peltier constant. At a thermocouple, i.e., a junction between two conductors with different Peltier coefficients, the heat current is not conserved, which implies heating or cooling depending on the current direction.[1,2] The thermopower, on the other hand, is the thermoelectric voltage that is generated by a temperature difference over a metal wire that is proportional to the Seebeck coefficient. A thermocouple generates an isothermal thermoelectric voltage proportional to the difference between the Seebeck coefficients when the end of the wires are maintained at a temperature different from the junction. Nanostructured materials can enhance the efficiency of thermoelectric devices.[3] The thermoelectric effects in metallic heterostructures including ferromagnets depend on the spin degree of freedom.[4] The spin dependence of thermoelectric cooling[5–7] is part of the field that studies the coupling between spin, heat, and electric transport in small structures and devices or spin caloritronics.[8] Heating is an important issue for spin torque magnetic random access memories (STT-MRAM) device [MRAM], and spin caloritronic effects can improve their performance.[9]

An enhanced Peltier effect has been reported by Fukushima *et al.*[10–12] in metallic multilayers when structured into nanopillars. The effect was detected by a change ΔR of the resistance R_0 as a function of current bias that acted as a thermometer. The Peltier effect cools or heats the systems by a term linear to the applied charge current I_c and Peltier coefficient Π, while the Joule heating induces a temperature and resistance change that scales like the square of the current bias such that $\Delta R \sim R_0 I_c^2 - \Pi I_c$. At small currents, the linear term dominates and causes a reduction of the resistance, i.e., an effective cooling, that in some structures was found to be very large. The Peltier coefficient was found by measuring the current where heating and cooling compensate each other and $\Delta R(I_c^{(0)}) = 0$ and therefore $\Pi = R_0 I_c^{(0)}$. The observed $\Pi = 480$ mV in pillars containing Constantan (CuNi) is attractive for cooling nanoelectronic devices.[12] The cooling power enhancement was tentatively explained by Yoshida *et al.*[13,14] by an adiabatic spin-entropy expansion. However, such an equilibrium cooling mechanism could not explain that Π is material dependent and even changes sign. The diffusion equation approach by Hatami *et al.*[5] did not take into account either the precise sample configuration or Joule heating and could not reproduce the large observed effects. The physical mechanism of the giant Peltier effect therefore remains unexplained. On the other hand, the recent experiments by Bosu *et al.*[15] confirmed the large Peltier coefficients for pillars including Heusler alloys when becoming very narrow. The present research has been motivated by the wish to model the heat and charge currents realistically in the hope to shed light onto this quandary. We report detailed calculations for the structure and model parameters matching Bosu *et al.*[15] experiments and compare the results of semi-analytic calculations with experiments. This study is limited to the thermoelectric effects as described by the two-current model of thermoelectric transport in which spin current is carried by particle currents. We do not include explicitly phonon contributions to the heat current as well as phonon/magnon drag effects on the thermoelectric coefficients, which may lead to a temperature dependence of the model parameters. Furthermore, we completely disregard collective effects that give rise to, e.g., the spin Seebeck and spin Peltier effects.[8] There are no indications that these approximations will do more than leading to some renormalization of the model parameters. While we are still far from a complete understanding of the experiments, we find evidence that very thin (Ohmic) tunnel junctions can enhance the Peltier effect.

This paper is organized as follows. In Section II, we review the standard Valet-Fert model for spin transport[16] in

our nanopillars, with explicit inclusion of interfaces. In Sec. III, we extend the model to include heat currents, charge and spin Joule heating and explain our method to compute temperature profiles. In Sec. IV, we present results for the Peltier effect due to different interfacial thermoelectric parameters and simulations of the Peltier effect are also performed, illustrating the importance of interface resistances, to finish in Sec. V with a summary and conclusions.

II. SPIN-DEPENDENT DIFFUSION IN F|N|N_B MODEL

Our model can be applied quite generally to arbitrary multilayered structures, but we focus here on the charge-current biased trilayer nanostructures measured by Bosu *et al.*[15] that are composed of a ferromagnetic metal F and two normal metals N and N_B, respectively, as sketched in Fig. 1. The thicknesses of F, N, and N_B are L_F, L, and L_B, consecutively, and the device is sandwiched between two thermal reservoirs at the same temperature T_0. The electric, spin, and heat transport are described by an extended Valet-Fert model,[16] including interfaces[17] and spin-dependent thermoelectric effects.[5] The parameters are the resistances R_1 and R_2 for the F|N and N|N_B interfaces, respectively,[18,19] the bulk resistance R_i ($i = $ F, N, N_B) for each metal, as well as the spin polarization P_F of the ferromagnetic metal.

We adopt a one-dimensional diffusion model in which the currents flow along the x-direction and the origin is at the F|N interface. In the collinear two-channel resistor model, the electrons are either in the spin-up or spin-down states. We divide the structure into various elements such as resistors, nodes, and reservoirs. Discrete resistive elements are interfaces, tunnel barriers, or constrictions that limit the transport. For our purpose, resistors are separated by nodes in which electrons can be described semiclassically by distribution functions f_i. If the interactions electron-electron or electron-phonon are sufficiently strong, f_i approaches the Fermi-Dirac distribution which depends on temperatures T_i and chemical potentials μ_i. We disregard spin-dependent temperatures here[5] but allow for spin accumulations, i.e., local differences between chemical potentials for both spins.

The spin diffusion approximation is well established for metallic magnetic multilayers, since its anticipation by Valet and Fert[16] for spin and charge transport for the CPP GMR (current perpendicular to the plane giant magnetoresistance) and withstood the test of time over many years. We are

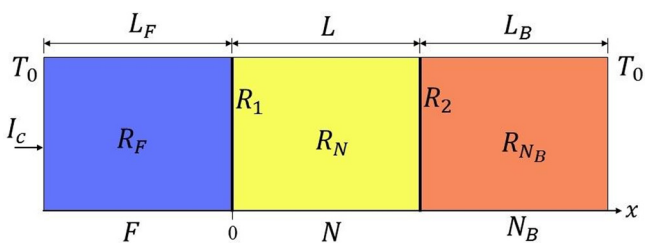

FIG. 1. F|N|N_B nanopillar structure biased with a charge current I_c. We consider a nanopillar with cross section A_c. F, N, and N_B represent a ferromagnetic metal, a normal metal spacer, and a normal metal B, respectively. L_F, L, and L_B are the thicknesses of each section. The ends of the nanostructure are connected to thermal reservoirs kept at a constant temperature T_0.

therefore confident that its generalization which includes thermoelectric effects as originally proposed by Johnson and Silsbee[4] and later formulated by Hatami *et al.*[5] is robust as well. The formalism should be valid as long as the high metal electron density and the interface/bulk disorder prevent significant quantum effects on transport. We are not aware of transport experiments in metallic multilayers that seriously challenge the semiclassical spin diffusion model.

The spin particle $I_c^{(\alpha)}$ and heat $J_q^{(\alpha)}$ currents at a position x in a resistive element are[20]

$$I_c^{(\alpha)} = A_c \int d\epsilon j^{(\alpha)}(\epsilon, x), \tag{1}$$

and

$$J_q^{(\alpha)} = -\frac{1}{e}\int d\epsilon \epsilon j^{(\alpha)}(\epsilon, x) - \mu_0 \int d\epsilon j^{(\alpha)}(\epsilon, x), \tag{2}$$

respectively, where A_c is the cross sectional area of the nanopillar, $\alpha = \uparrow(\downarrow)$ is the electron spin degree of freedom, $j^{(\alpha)}$ is the spin, energy (ϵ), and position (x) dependent spectral current density, and μ_0 is the ground-state chemical potential. $j^{(\alpha)} = \sigma^{(\alpha)}(\epsilon) f^{(\alpha)}(\epsilon, x)$ is described by local Fermi-Dirac distributions $f^{(\alpha)}$ at temperature T and spin-dependent chemical potentials μ^{α}, times the energy-dependent conductivity $\sigma^{\alpha}(\epsilon)$.

The spin accumulation is defined as $\mu_s = \mu_\uparrow - \mu_\downarrow$, where $\mu_{\uparrow,\downarrow}$ are the spin-up and spin-down chemical potentials, while the charge chemical potential is the average $\mu_c = (\mu_\uparrow + \mu_\downarrow)/2$.

The transport in each layer is governed by the spin and charge diffusion equations,[16] given by

$$\frac{\partial^2}{\partial x^2}\mu_s = \frac{\mu_s}{\lambda^2}, \tag{3}$$

$$\frac{\partial^2}{\partial x^2}\mu_c = -P_F \frac{\mu_s}{2\lambda^2}, \tag{4}$$

where λ is the spin-flip diffusion length, usually much larger in normal metals than in ferromagnetic metals $\lambda_{N,N_B} \gg \lambda_F$, and

$$P_F = \frac{\sigma_F^{\uparrow} - \sigma_F^{\downarrow}}{\sigma_F^{\uparrow} + \sigma_F^{\downarrow}}, \tag{5}$$

is the transport spin polarization in terms of the spin-dependent conductivities for each channel in the ferromagnet. In the normal metals, N and N_B, these polarizations vanish ($P_{N,N_B} = 0$). The solution of Eq. (3),

$$\mu_s = Y e^{\frac{x}{\lambda}} + Z e^{-\frac{x}{\lambda}}, \tag{6}$$

depends on the integration constants Y and Z. For a ferromagnetic metal F,[21] we find (see Fig. 1)

$$\frac{\mu_F^{(\alpha)}(x)}{e} = -\frac{I_c}{\sigma_F A_c}x + \alpha_1 \pm \frac{\sigma_F}{\sigma_F^{\alpha}}\beta_1 e^{\frac{x}{\lambda_F}}, \tag{7}$$

where α_1 is the voltage drop at the F|N interface, σ_F is the electrical conductivity of the ferromagnetic metal, σ_F^{α} is the spin-dependent conductivity, λ_F is the spin-flip diffusion

length and β_1 is a coefficient to be determined by boundary conditions at the interfaces.[17]

For the normal metals, the spin-up and spin-down chemical potentials read

$$\frac{\mu_N^{(\alpha)}(x)}{e} = -\frac{I_c}{\sigma_N A_c}x \pm b_1 e^{-\frac{x}{\lambda_N}} \pm b_2 e^{\frac{x}{\lambda_N}}, \tag{8}$$

$$\frac{\mu_{N_B}^{(\alpha)}(x)}{e} = -\frac{I_c}{\sigma_{N_B} A_c}(x-L) + \alpha_2 \pm c_1 e^{-\frac{x-L}{\lambda_{N_B}}} \pm c_2 e^{\frac{x-L}{\lambda_{N_B}}}, \tag{9}$$

for N and N_B, respectively, where b_1, b_2, c_1, and c_2 complete the number of coefficients that describe the spin-dependent transport in the present trilayer system. The spin accumulations, in each layer of the F|N|N_B nanowire, are $\mu_s^X(x)$, while the charge chemical potentials read $\mu_c^X(x)$, and the spin-dependent currents[22] in a bulk ferromagnetic metal are (Ohm's Law)

$$I_X^{(\alpha)}(x) = -A_c \sigma_X^{(\alpha)} \frac{\nabla \mu_X^{(\alpha)}(x)}{e}, \tag{10}$$

where $X = F$, N, and N_B and $\sigma_N^{(\alpha)} = \sigma_N/2$. The spin current $I_X^s = I_X^{(\uparrow)} - I_X^{(\downarrow)}$ is the difference between spin-up and spin-down currents where the parameters such as $R_{\lambda_X} = \rho_X \lambda_X / A_c$, which is the resistance over the spin-flip diffusion length λ_X in X, and the corresponding electrical resistivity ρ_X, are implicit in the calculations.

A. Interface resistances

Next, we consider spin-dependent transport through the interfaces. We disregard interface-induced spin-flips,[19] so that at the F|N interface[18]

$$I_1^{(\alpha)} = \frac{G_1^{(\alpha)}}{e}\left[\mu_F^{(\alpha)}(0) - \mu_N^{(\alpha)}(0)\right], \tag{11}$$

where $G_1^{(\alpha)}$ is the interface conductance with polarization $P_1 = (G_1^{(\uparrow)} - G_1^{(\downarrow)})/G_1$ and $G_1 = G_1^{(\uparrow)} + G_1^{(\downarrow)}$. At the interface between the two normal metals N|N_B

$$I_2^{(\alpha)} = \frac{G_2^{(\alpha)}}{e}\left[\mu_N^{(\alpha)}(L) - \mu_{N_B}^{(\alpha)}(L)\right]. \tag{12}$$

Charge current $I_c = I_{1,2} = I_{1,2}^{(\uparrow)} + I_{1,2}^{(\downarrow)}$ and spin current $I_{1,2}^s = I_{1,2}^{(\uparrow)} - I_{1,2}^{(\downarrow)}$ are conserved at the interfaces 1 and 2, assuming that $R_1 = 1/G_1$ and $R_2 = 1/G_2$.

B. Boundary conditions

The boundary conditions are spin and charge current conservation at the interfaces

$$I_F^s(0) = I_N^s(0) = I_1^s, \tag{13}$$

for the F|N interface and

$$I_N^s(L) = I_{N_B}^s(L) = I_2^s, \tag{14}$$

for the N|N_B interface. We assume that the spin accumulation vanishes at the end of N_B so that

$$\mu_{N_B}^s(L + L_B) = 0, \tag{15}$$

which is valid for $L_N \gg \lambda_N$ or $L_B \gg \lambda_{N_B}$ and/or when the nanopillar diameter widens at L_B. We can now numerically determine the coefficients β_1, b_1, b_2, c_1, and c_2 and thereby spin accumulation, spin current, and charge chemical potential can be now computed.

The total electrical resistance, $R = \mu_c/(eI_c)$

$$R = R_{F|N|N_B} = R_F(x = -L_F) - R_{N_B}(x = L + L_B), \tag{16}$$

$$R(T_0) = -\frac{2P_F}{I_c(1-P_F^2)}\beta_1 e^{L_F/\lambda_F} + \frac{\alpha_1}{I_c} - \frac{\rho_F L_F}{A_c} - \frac{\alpha_2}{I_c} + \frac{\rho_{N_B} L_B}{A_c}, \tag{17}$$

where

$$\alpha_1 = I_c R_1 - \frac{2\beta_1(P_1 - P_F)}{(1-P_F^2)} + P_1(b_1 + b_2), \tag{18}$$

and

$$\alpha_2 = -I_c R_2 - \frac{I_c \rho_N L}{A_c}, \tag{19}$$

are the voltage drops at the interfaces 1 and 2, respectively.

Numerical results for the transport properties require to consider the parameters of the samples of Bosu *et al.*[15] at room temperature T_0. The ferromagnetic metal is typically a Heusler alloy Co_2MnSi (CMS),[23] while the normal metal N is gold and N_B is Cu. The resistivities and spin-flip diffusion lengths are given in Table I.

Fig. 2 illustrates that a charge current I_c leads to a spin accumulation over the spin-flip diffusion length λ_F in F, reaching its maximum value at the F|N interface, where the spin is injected[6,22,28,29] and decays exponentially on the scale of the spin-flip diffusion lengths of the normal metals λ_{N,N_B}. The spin current as plotted in Fig. 3 is proportional to the gradient of the spin accumulation (Eq. (10)). We observe that it decays rapidly in the ferromagnet close to the interface and also in the central island, reflecting that in our devices $\lambda_F < \lambda_{Au} < \lambda_{Cu}$. Additionally, the design parameters L and L_B are important via the boundary condition Eq. (15).

III. SPIN-DEPENDENT THERMOELECTRICITY OF F|N|N_B PILLARS

In the experiments, the electrical resistance change is measured as a function of an applied current, reflecting

TABLE I. Spin-flip diffusion lengths and electrical resistivities at 300 K used for the F|N|N_B nanopillar structure.[15,23,30–33]

Material	λ (nm)	ρ ($\mu\Omega$ cm)
Co_2MnSi	2.1	70.0
Au	60	2.27
Cu	350	1.73

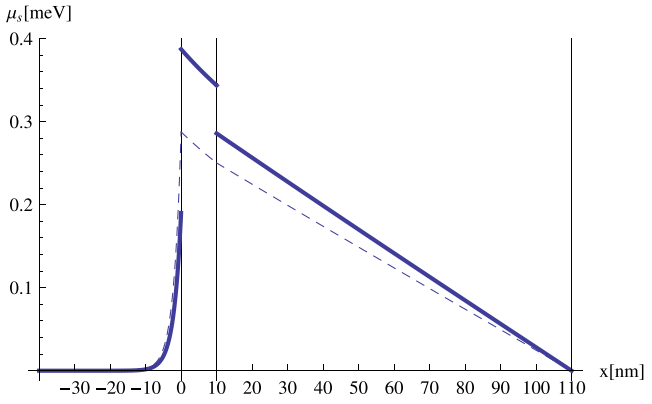

FIG. 2. Spin accumulation in a Co_2MnSi(CMS)[40 nm]|Au[10 nm]|Cu [100 nm] nanopillar with diameter $D = 180$ nm for a current $I_c = 5$ mA and taking interface resistances[24,25] into account $A_cR_1 = 0.915 \times 10^{-15}\,\Omega m^2$ (Ref. 26) and $A_cR_2 = 3.40 \times 10^{-16}\,\Omega m^2$ at 300 K, the polarization of ferromagnetic metal is $P_F = 0.71$ and the polarizations of the interfaces[27] are $P_1 = 0.77$ and $P_2 = 0$. The dashed lines show the spin accumulation when interface resistances A_cR_1 and A_cR_2 are set to zero (metallic contact).

the balance between the Joule heating and Peltier cooling. In order to model this effect, we need to compute the temperature profile $T(x)$ over F|N|N_B pillars. Temperature distributions have been previously calculated, without taking Joule heating into account in spin-dependent systems.[20] Assuming that we know the temperature dependence of the electrical resistivity $\rho(T)$ and the interface resistances $R_{1,2}(T)$, the total temperature dependent resistance reads

$$\Delta R = \frac{1}{L}\int R[T(x)]dx - R(T_0), \tag{20}$$

where $R(T_0)$ is given in Eq. (17). For simplicity, we disregard the heat leakage through the cladding of the nanopillar, which is valid when the thermal contact is weak or the cladding material has a much smaller heat conductivity. Significant heat leakage would reduces the temperature gradients calculated here, leading to an overestimation of

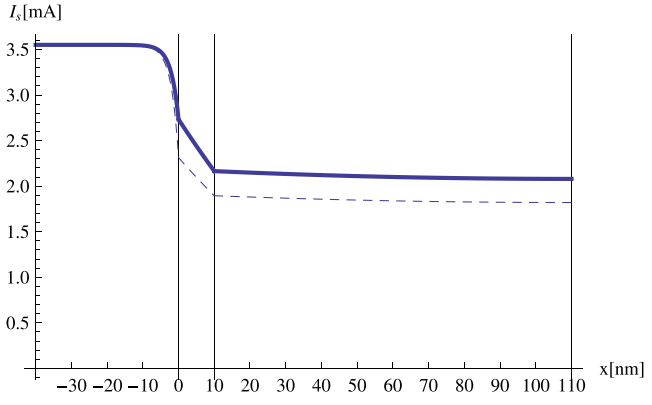

FIG. 3. Spin current in the CMS[40 nm]|Au[10 nm]|Cu[100 nm] nanopillar structure for a charge current bias $I_c = 5$ mA and taking interface resistances into account. The dashed line is the spin current when interface resistances A_cR_1 and A_cR_2 are set to zero (metallic contact).

the thermoelectric cooling power. In the following, we determine the heat current and its divergence in the nanopillar taking into account the Kapitza thermal resistances at interfaces.[34] The temperature profile in the nanopillar structure is calculated using heat conservation at interfaces. This allows us to describe the performance of the nanodevice by the resistance-current (R-I) characteristics. Except for the temperature dependence of the resistance that serves as a thermometer, we disregard here the weak temperature and voltage dependences of the thermoelectric parameters.

In the Sommerfeld approximation, the linear response relations between currents and forces in bulk materials read[20]

$$\begin{pmatrix} J_c \\ J_s \\ J_q \end{pmatrix} = \sigma \begin{pmatrix} 1 & P_F & ST \\ P_F & 1 & P'_F ST \\ ST & P'_F ST & \kappa T/\sigma \end{pmatrix} \begin{pmatrix} -\partial_x \mu_c/e \\ -\partial_x \mu_s/(2e) \\ -\partial_x \ln T \end{pmatrix}, \tag{21}$$

where S is the (charge) Seebeck coefficient, σ is the electrical conductivity, κ is the thermal conductivity, all at the Fermi energy, and T is the temperature (disregarding spin temperatures[35]). Here, $J_c \equiv I_c/A_c$, etc., are current densities

$$P'_F = \frac{\frac{\partial}{\partial E}\left(\sigma_F^{\uparrow} - \sigma_F^{\downarrow}\right)_{E_F}}{\frac{\partial}{\partial E}\left(\sigma_F^{\uparrow} + \sigma_F^{\downarrow}\right)_{E_F}}, \tag{22}$$

is the spin polarization of the energy derivative of the conductivity at the Fermi energy, which is related to the spin polarization of the thermopower as

$$P_S \equiv \frac{S_{\uparrow} - S_{\downarrow}}{S_{\uparrow} + S_{\downarrow}} = \frac{P'_F - P_F}{1 - P'_F P_F}. \tag{23}$$

Joule heating is a source term that causes a divergence in the heat current[36]

$$\frac{\partial}{\partial x} J_q = -J_c \frac{\partial}{\partial x}\frac{\mu_c}{e}. \tag{24}$$

Including the dissipation due to the spin relaxation,[35,37] we obtain the matrix expression for the divergence of the current densities

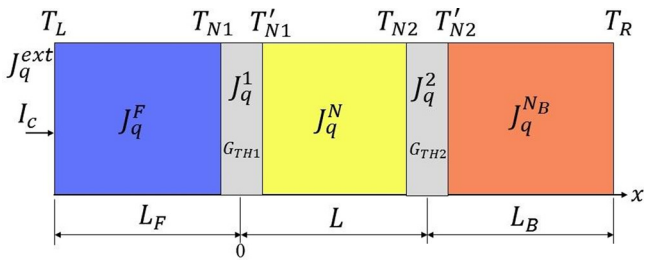

FIG. 4. Definition of temperatures and heat currents in $F|N|N_B$ nanopillar structures along the x-direction, including Kapitza thermal conductances $G_{TH1,2}$.

$$\frac{\partial}{\partial x}\begin{pmatrix} J_c \\ J_s \\ J_q \end{pmatrix} = \begin{pmatrix} 0 & 0 & 0 \\ 0 & -\dfrac{1-P_F^2}{2\rho\lambda^2} & 0 \\ -J_c\dfrac{\partial}{\partial x} & -J_s\dfrac{\partial}{2\partial x} & 0 \end{pmatrix}\begin{pmatrix} \mu_c/e \\ \mu_s/e \\ T \end{pmatrix}. \quad (25)$$

A. Heat currents and temperature profiles in the bulk of the layers

The divergence of the heat current in the ferromagnet F reads (Eq. (25))

$$\frac{\partial}{\partial x}J_q^F = J_c^2\rho_F + \frac{(1-P_F^2)\mu_s^2}{4e^2\rho_F\lambda^2} + \frac{J_q^2}{\kappa}, \quad (26)$$

which equals the derivative of the heat current in Eq. (21)

$$\frac{\partial}{\partial x}J_q^F = \frac{\partial}{\partial x}\left(J_c S_F T - \frac{(P_F' - P_F)S_F T\mu_s}{2e\rho_F\lambda} - \kappa_F\frac{\partial}{\partial x}T\right), \quad (27)$$

$$= -\frac{(P_F' - P_F)S_F T}{\rho_F}\frac{\mu_s}{2e\lambda^2} - \kappa_F\frac{\partial^2}{\partial x^2}T, \quad (28)$$

leading to the heat diffusion equation

$$\frac{\partial^2}{\partial x^2}T = -\frac{(P_F' - P_F)S_F T}{\rho_F\kappa_F}\frac{\mu_s}{2e\lambda^2} - \frac{J_c^2\rho_F}{\kappa_F} - \frac{(1-P_F^2)\mu_s^2}{4e^2\rho_F\kappa_F\lambda^2} - \frac{J_q^2}{\kappa_F^2}. \quad (29)$$

Heat transport is carried in parallel by phonons and electrons.[38] We assume here the efficient thermalization in and between both subsystems, meaning that the electron and phonon temperatures are taken to be identical. The total thermal conductivity then reads $\kappa = \kappa_e + \kappa_p$.

For the ferromagnetic metal F, we set $T(x=0) = T_{N1}$, where T_{N1} is governed by the boundary condition at the F|N interface discussed in Subsection III B, while $T(x=-L_F) = T_L$ is fixed by the reservoir (see Fig. 4). The solution of the heat diffusion Eq. (29) disregarding the generalized Thomson effect term $-J_q^2/\kappa^2$ then becomes

$$\begin{aligned} T_F(x) = &-\frac{2(P_F' - P_F)S_F T\beta_1}{\kappa_F\rho_F(1-P_F^2)}\left[e^{\frac{x}{\lambda_F}} - 1\right] - \frac{I_c^2\rho_F x^2}{2\kappa_F A_c^2} \\ &-\frac{\beta_1^2}{\kappa_F\rho_F(1-P_F^2)}\left[e^{\frac{2x}{\lambda_F}} - 1\right] + T_{N1} \\ &+\frac{x}{L_F}\left(T_L - T_{N1} + \frac{2(P_F' - P_F)S_F T\beta_1}{\kappa_F\rho_F(1-P_F^2)}\left[e^{\frac{x}{\lambda_F}} - 1\right]\right. \\ &\left.+\frac{I_c^2\rho_F x^2}{2\kappa_F A_c^2} + \frac{\beta_1^2}{\kappa_F\rho_F(1-P_F^2)}\left[e^{\frac{2x}{\lambda_F}} - 1\right]\right), \end{aligned} \quad (30)$$

and

$$\begin{aligned} \frac{\partial}{\partial x}T_F = &-\frac{2(P_F' - P_F)S_F T\beta_1}{\kappa_F\rho_F(1-P_F^2)}\left(e^{\frac{x}{\lambda_F}}\lambda_F - \frac{\left[e^{\frac{L_F}{\lambda_F}} - 1\right]}{L_F}\right) \\ &-\frac{\beta_1^2}{\kappa_F\rho_F(1-P_F^2)}\left(\frac{2e^{\frac{2x}{\lambda_F}}}{\lambda_F} - \frac{\left[e^{\frac{2L_F}{\lambda_F}} - 1\right]}{L_F}\right) \\ &-\frac{I^2\rho_F}{\kappa_F A_c^2}\left(x - \frac{L_F}{2}\right) + \left(\frac{T_L - T_{N1}}{L_F}\right). \end{aligned} \quad (31)$$

Finally, the heat current distribution reads

$$\begin{aligned} J_q\cdot A_c = &S_F T I_c + \frac{2(P_F' - P_F)S_F T\beta_1}{(1-P_F^2)}\left(\frac{1-e^{\frac{2L_F}{\lambda_F}}}{R_F}\right) \\ &+\frac{\beta_1^2}{(1-P_F^2)}\left(\frac{2e^{\frac{2x}{\lambda_F}}}{R_{\lambda_F}} + \frac{1-e^{\frac{2L_F}{\lambda_F}}}{R_F}\right) \\ &+I_c^2\left(R_F\frac{x}{L_F} - \frac{R_F}{2}\right) - \frac{\kappa_F A_c}{L_F}(T_L - T_{N1}), \end{aligned} \quad (32)$$

where $R_F = \rho_F L_F/A_c$ is the electrical and $R_{\lambda_F} = \rho_F\lambda_F/A_c$ is the spin resistance.

Repeating this analysis for normal metals, we obtain a heat current in N

$$\begin{aligned} J_q^N(x)\cdot A_c = &S_N T I_c + I_c^2\left(R_N\frac{x}{L} - \frac{R_N}{2}\right) \\ &-b_1^2\left(\frac{e^{-\frac{2x}{\lambda_N}}}{2R_{\lambda_N}} + \frac{\left[e^{-\frac{2L}{\lambda_N}} - 1\right]}{4R_N}\right) \\ &+b_2^2\left(\frac{e^{\frac{2x}{\lambda_N}}}{2R_{\lambda_N}} - \frac{\left[e^{\frac{2L}{\lambda_N}} - 1\right]}{4R_N}\right) \\ &-\frac{b_1 b_2}{R_{\lambda_N}}\left(\frac{2x-L}{\lambda_N}\right) - \frac{\kappa_N A_c}{L}\left(T_{N2} - T_{N1}'\right), \end{aligned} \quad (33)$$

and in N_B

$$\begin{aligned} J_q^{N_B}(x)\cdot A_c = &S_{N_B} T I_c + \frac{I_c^2\rho_{N_B}}{A_c}\left(x - \frac{2L+L_B}{2}\right) \\ &-c_1^2\left(e^{-2\frac{x-L}{\lambda_{N_B}}}2R_{\lambda_{N_B}} + \frac{e^{-2\frac{L_B}{\lambda_{N_B}}} - 1)}{4R_{N_B}}\right) \\ &+c_2^2\left(\frac{e^{2\frac{x-L}{\lambda_{N_B}}}}{2R_{\lambda_{N_B}}} - \frac{e^{2\frac{L_B}{\lambda_{N_B}}} - 1}{4R_{N_B}}\right) \\ &-\frac{c_1 c_2}{R_{\lambda_{N_B}}}\left(\frac{2x}{\lambda_{N_B}} - \frac{2L+L_B}{\lambda_{N_B}}\right) - \frac{\kappa_{N_B} A_c}{L_B}\left(T_R - T_{N2}'\right), \end{aligned} \quad (34)$$

B. Interfaces

Finally, we knit the solutions for the bulk layers together at the interfaces by boundary conditions. The

contacts to an abruptly widening nanopillar may be treated as ideal reservoirs (heat and spin sinks) at constant temperatures $T_L = T_R = T_0$ (see Fig. 4). By disregarding interface-induced spin-flips[19] and, for the moment, the Joule heating by the interface resistance, we may impose charge, spin, and energy conservation at each interface,[11,39,40] such as $J_q^F(x=0) = J_q^1 = J_q^N(x=0)$ for F|N, and analogously to Eq. (21)[34]

$$J_q^1 \cdot A_c = G_{\mathrm{TH1}} A_c \Delta T - G_1 S_1 T_1 \Delta\mu_c^{(1)} - P_F' G_1 S_1 T_1 \frac{\Delta\mu_s^{(1)}}{2}, \tag{35}$$

where J_q^1 is the interface heat current, G_{TH1} is the Kapitza thermal conductance (including the phonon contribution), A_c is the cross sectional area of the nanopillar, $\Delta T = T_{N1} - T_{N1}'$ is the temperature drop over the interface, $T_1 = (T_{N1} + T_{N1}')/2$ is the interface temperature, G_1 is the electrical interface conductance, S_1 is the interface thermopower, and $\Delta\mu_{c(s)}^{(1)}$ are the charge (spin) accumulation differences over the interface.

Substituting Eqs. (32) and (33) for $x = 0$ leads to

$$\begin{aligned} T_{N1} = {} & \left\{ -\left(S_N I_c + \frac{\kappa_N A_c}{L}\right)\left(-\frac{\kappa_F A_c T_L}{H_2 L_F} - \frac{I_c^2 R_F}{2H_2} + \frac{\beta_1^2}{H_2(1-P_F^2)}\left(\frac{2}{R_{\lambda_F}} - \frac{e^{\frac{2L_F}{\lambda_F}}-1}{R_F}\right)\right) - \frac{I_c^2}{2}(R_F - R_N) - \frac{\kappa_F A_c T_L}{L_F} + \frac{\kappa_N A_c T_{N2}}{L} \right. \\ & + \frac{\beta_1^2}{(1-P_F^2)}\left(\frac{2}{R_{\lambda_F}} - \frac{e^{\frac{2L_F}{\lambda_F}}-1}{R_F}\right) + b_1^2\left(\frac{1}{2R_{\lambda_N}} + \frac{\left[e^{-\frac{2L}{\lambda_N}}-1\right]}{4R_N}\right) - b_2^2\left(\frac{1}{2R_{\lambda_N}} - \frac{\left[e^{\frac{2L}{\lambda_N}}-1\right]}{4R_N}\right) + \frac{b_1 b_2}{R_{\lambda_N}}\left(\frac{-L}{\lambda_N}\right) \Bigg\} \Bigg/ \\ & \left\{ \left(S_N I_c + \frac{\kappa_N A_c}{L}\right)\left(\frac{S_F I_c}{H_2} + \frac{\kappa_F A_c}{H_2 L_F} + \frac{2(P_F' - P_F) S_F \beta_1}{H_2(1-P_F^2)}\left(-\frac{\left[e^{\frac{L_F}{\lambda_F}}-1\right]}{R_F}\right) - \frac{H_1}{H_2}\right) - S_F I_c - \frac{\kappa_F A_c}{L_F} \right. \\ & \left. - \frac{2(P_F' - P_F) S_F \beta_1}{(1-P_F^2)}\left(-\frac{\left[e^{\frac{L_F}{\lambda_F}}-1\right]}{R_F}\right) \right\}, \end{aligned} \tag{36}$$

and

$$T_{N1}' = \left(\frac{S_F I_c}{H_2} + \frac{\kappa_F A_c}{H_2 L_F} + \frac{2(P_F' - P_F) S_F \beta_1}{H_2(1-P_F^2)}\left(-\frac{\left[e^{\frac{L_F}{\lambda_F}}-1\right]}{R_F}\right) - \frac{H_1}{H_2}\right) T_{N1} - \frac{\kappa_F A_c T_L}{H_2 L_F} - \frac{I_c^2 R_{F_L}}{2H_2} + \frac{\beta_1^2}{H_2(1-P_F^2)}\left(\frac{2}{R_{\lambda_F}} - \frac{\left[e^{\frac{2L_F}{\lambda_F}}-1\right]}{R_F}\right), \tag{37}$$

where $H_{1(2)} = -G_1 S_1 \Delta\mu_c^{(1)}/2 - P_F' G_1 S_1 \Delta\mu_s^{(1)}/4 \pm G_{\mathrm{TH1}} A_c$. We may determine the temperatures T_{N2} and T_{N2}' at interface N|N$_B$ analogously.

Eqs. (36) and (37) include bulk and interfacial Peltier effects as well as Joule heating in the bulk materials (see Fig. 4) but not yet the interfacial Joule heating. Here, we focus on Joule heating by the N|N$_B$ interface, which is the dirty one in the experiments.[12,15] We can treat the interface heating easily in two limiting cases. In the dirty limit, the interface is a resistor with a small but finite thickness L_I around the position $x = d_I$ in which the electrons dissipate their energy directly to the lattice

$$\frac{\partial}{\partial x} J_q^I = \begin{cases} J_c^2 \dfrac{R_I A}{L_I} & \text{for } -L_I/2 < x - d_I < L_I/2 \\ 0 & \text{otherwise.} \end{cases} \tag{38}$$

Clean interfaces, point contacts, or coherent tunnel junctions, on the other hand, inject hot electrons (and holes) into the neighboring layers where they loose their excess energy on the scale of the electron-phonon thermalization length λ^{ep}. In normal metals like Cu, it is surprisingly large even at room temperature, i.e., $\lambda_{Cu}^{ep} = 60\,\mathrm{nm}$.[35] In the clean limit (assuming that $\lambda_A^{ep} + \lambda_B^{ep}$ is smaller than the pillar length),

$$\frac{\partial}{\partial x} J_q^I = \begin{cases} J_c^2 \dfrac{R_I A}{\lambda_A^{ep} + \lambda_B^{ep}} & \text{for } -\lambda_A^{ep} < x - d_I < \lambda_B^{ep} \\ 0 & \text{otherwise.} \end{cases} \tag{39}$$

The two limits therefore differ only by the volume in which the heat is produced. In the extreme case of $\lambda_A^{ep} \gg L_X$, all interface Joule heating occurs in the reservoirs, where its effect can be disregarded. In the following, we consider both

extremes, i.e., the dissipation occurs either in the interfacial thickness L_I or in the reservoirs $\lambda_A^{ep} + \lambda_B^{ep} = \infty$.

We can implement these models into Eqs. (36) and (37) as follows. In Eqs. (38) and (39), the Joule heating is represented by the power density $J_c^2 R_I A/L_I$ in the volume $V = AL_I$. The total power dissipated at the interface is therefore $I_c^2 R_I$. This term can be added to Eq. (36); the first term of the third line expresses the balance between the Joule heating of the bulk metals to which the interface contribution may be added. The interfacial Joule heating thereby reduces the cooling power of the nanopillar. By contrast, in the ballistic limit with long relaxation lengths, the Joule heating is deferred to the heat sinks and does not contribute at all.

IV. RESULTS

In general, interfacial resistances $R_{1/2}$ may vary from close to zero for good metallic contacts to that of a very thin (Ohmic) tunnel barrier. A highly resistive interface can, e.g., be caused by a sample fabrication process in which the vacuum is broken, leading to organic deposits.[12,15] We can simulate resistive F|N or N|N_B interfaces by modulating $R_{1,2}$ from zero resistance to a large value. A large resistance of either interface turns out to enhance the cooling effect as long as the interfacial Joule heating does not dominate, i.e., when the current bias is not too large.

A. Temperature profiles in a F|N|N_B pillar

We are interested in the temperature profile of a pillar with equal temperatures of the two external reservoirs $T_L = T_R = T_0$, noting that the model can be easily extended to calculate the thermopower due to a global temperature difference over the device. We start with $T_{N1} = T'_{N1} = T_{N2} = T'_{N2} = T_0$ as initial conditions (see Fig. 4), which are substituted into Eqs. (36) and (37) to obtain a first iteration. The temperature profiles converge after several iterations.

Results are shown in Fig. 5 for different current densities, with temperature T_0 in the reservoirs maintained at 300 K, using the parameters from Tables I–III for bulk and interfaces. We adopt here the ballistic model Eq. (39) with long relaxation lengths, in which interface-induced Joule heating occurs along its interfacial thickness. The top panel of Fig. 5 is the resulting temperature profile with clean interfaces of $A_c R_1 = 0.915\,\mathrm{f\Omega m^2}$ and $A_c R_2 = 0.34\ \mathrm{f\Omega m^2}$ (see the values of interface parameters in Table III). The interfacial electrical conductances are relatively well-known parameters, in contrast to the Kapitza heat conductances G_{TH}. The Joule heating is generated mainly by the relatively resistive ferromagnetic metal, while the cooling takes place at the F|N interface, giving rise to a complex temperature and heat current distribution. The dotted lines for each curve show the average temperatures $T_{AV\,G}$ of the different layers that is used to compute the resistance change of the pillar.

The bottom panel of Fig. 5 shows the temperature profile in the presence of a highly resistive interface N|N_B with a 100 times larger resistance (increased to $A_c R_2 = 34\,\mathrm{f\Omega m^2}$). $G_{TH,2}$ is assumed to be reduced by the same factor to

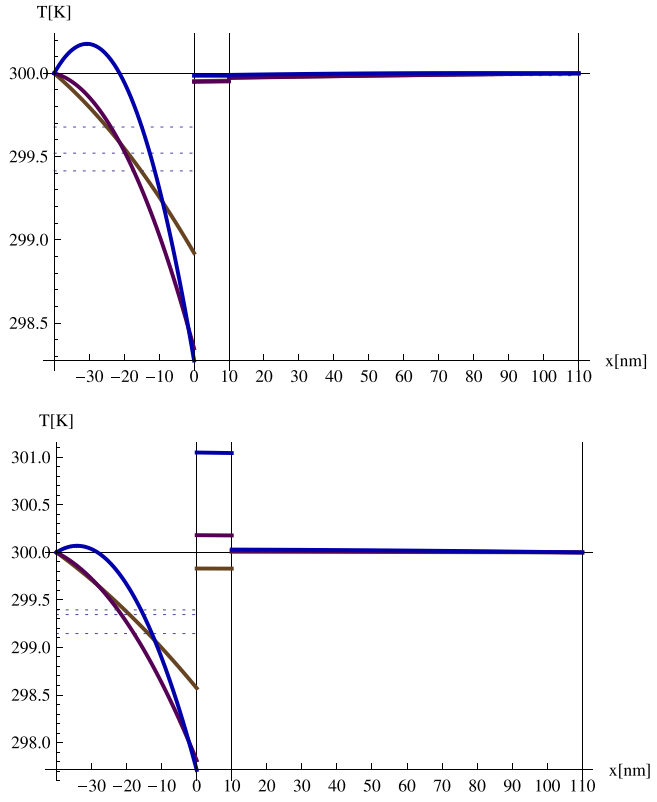

FIG. 5. Temperature distribution in a CMS[40 nm]|Au[10 nm]|Cu[100 nm] nanopillar under current bias for the thermoelectric parameters from Tables I–III and $T_0 = 300$ K. (Top) Clean interfaces with resistance area of $A_c R_1 = 0.915\,\mathrm{f\Omega m^2}$ and $A_c R_2 = 0.34\,\mathrm{f\Omega m^2}$. The brown, purple, and blue lines correspond to applied current densities of 1, 2, and $3 \times 10^{11}\,\mathrm{A/m^2}$, respectively. The dotted lines for each curve show the average temperatures in the different layers that govern the resistance change of the pillar. (Bottom) Temperature distribution in the presence of a dirty N|N_B interface with 100 times the electric (to $A_c R_2 = 34\,\mathrm{f\Omega m^2}$) and heat resistances, but otherwise the same parameters as above.

$5.9 \times 10^7\,\mathrm{W/m^2 K}$, while other parameters are kept the same. The dissipation at the dirty interface N|N_B is measured according to the expression of Eq. (38), which results in a local temperature increment of the normal metals for applied current densities greater than or equal to $2 \times 10^{11}\,\mathrm{A/m^2}$. A marked discontinuity of the temperature at the N|N_B interface develops due to the reduced thermal conductance $G_{TH,2}$. The temperature on the F-side drops from approximately 298.3 K for a clean N|N_B interface to 297.7 K for a dirty one (see Fig. 5). The increased interface resistance forms a barrier for the heat flow from the heat sinks towards the interface, allowing the region close to the interface to cool down more efficiently, thereby enhancing the effective Peltier effect.

B. Peltier cooling, Joule heating, and R-I characteristics

According to Eq. (20), the temperature profile $T(x)$ is directly related to the observable resistance change. We compute a specific temperature profile for a given current bias as sketched below, which can be used to obtain the total resistance as a function of current that may be directly

TABLE II. Thermoelectric parameters of the bulk metal layers in the F|N|N_B nanopillars at 300 K: Thermal conductivities κ (W/mK) and Seebeck coefficients S (μV/K). P_F is the polarization of the conductivity for the ferromagnet while P'_F is the polarization of its energy derivative. Due to lack of sufficient data, we take $P'_F - P_F = 0$, thereby disregarding much of the spin-dependence of the heat diffusion equations. R are the resistances in Ω when thicknesses L are in m.

Material	K	S	$P_F = P'_F$	$\partial R/\partial T$[15,30,33]
Co_2MnSi	15	−20	0.71	$6.07 \times 10^{-10} \cdot (L_F/A_c)$
Au (N)	318	1.83		$8.14 \times 10^{-11} \cdot (L/A_c)$
Cu (N_B)	401	1.94		$6.84 \times 10^{-11} \cdot (L_B/A_c)$

compared with the experimental results. To this end, we linearize Eq. (20) as

$$\Delta R_X \approx \frac{\partial R_X}{\partial T}\left(T_{X_{AVG}} - T_0\right). \tag{40}$$

The total resistance difference is governed by the temperature dependence of the layer and interface resistances. Each bulk material layer has a specific $\partial R_X/\partial T$, while the calculations establish average temperatures $T_{X_{AVG}}$ for the sections F, N, and N_B, respectively, as shown in Fig. 5 marked by dotted lines. Highly resistive interfaces may affect or even dominate the global resistance change when $R_{1(2)}$ and $\partial R_{1(2)}/\partial T$ are large. Our calculations include the temperatures at interfaces $T_{1(2)}$ as expressed in Eq. (35). For the temperature dependence of the bulk resistivities, we adopt the values listed in Table II. For resistive interfaces, we average $\partial R/\partial T$ of the two materials; for the N|N_B interface in Table III

$$\frac{\partial R_2}{\partial T} = \frac{1}{2}\frac{\partial (R_N + R_{N_B})}{\partial T}, \tag{41}$$

while we disregard the temperature dependence of the resistance for good interfaces.

In Fig. 6, the effect of inserting a highly resistive N|N_B interface on the R-I curves is shown for the non-local interface Joule heating scenario, i.e., when Eq. (39) is used with long relaxation lengths. The (effective) Peltier cooling (blue line, bottom) is visibly enhanced. The change in the total resistance can be understood in terms of the temperature distribution along the pillar as shown in Fig. 5. The increased interfacial resistance R_2 improves the effective Peltier coefficient from $\Pi = 11.2\,\text{mV}$ for a clean interface to $\Pi = 23.9\,\text{mV}$ in the case of a dirty interface. Additionally, a

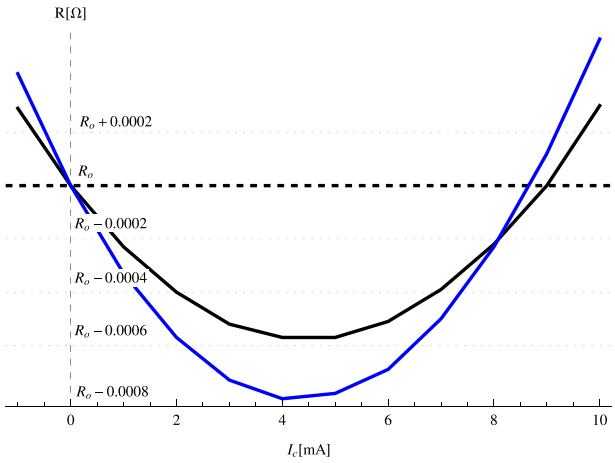

FIG. 6. Resistance-current relation of *CMS*[40 nm]|*Au*[10 nm]|*Cu*[100 nm] pillars including interface resistances as listed in Table II for the non-local interface Joule heating model. The effective Peltier coefficient is $\Pi = R_0 I_p = 1.25\,\Omega \times 8.95\,\text{mA} = 11.2\,\text{mV}$ (black line, top). The Peltier coefficient is increased to $\Pi = R_0 I_p = 2.76\,\Omega \times 8.7\,\text{mA} = 24\,\text{mV}$ (blue line, bottom) when a resistive N|N_B interface of $A_c R_2 = 34\,\text{f}\Omega\text{m}^2$ is inserted. Only for comparison purposes of the results in the present trilayer model, we mention that the conventional Peltier coefficient $\Pi_{CMS|Au}$ (considering only bulk metals without interface contribution) barely is 6 mV.

change in the Peltier coefficient from $\Pi = 23.9\,\text{mV}$ to $\Pi = 24\,\text{mV}$ is achieved by implementing Eq. (41). The highly resistive interface increases efficiency under a constant current bias, requiring a lower applied voltage for a larger cooling effect.

C. Trilayer nanopillar model

We now evaluate the thermoelectric performance as a function of structural and material parameters of the nanopillar. Matching samples of Bosu *et al.*,[15] we adopt bulk (Drude) thermopowers of the leads as $S_F = S_{CMS} = -20\,\mu\text{V/K}$ for the ferromagnetic Heusler alloy ($Co_2MnSi_{T_{ann}=500\text{K}}$), $S_{Au} = 1.83\,\mu\text{V/K}$ for the normal metal N, and $S_{Cu} = 1.94\,\mu\text{V/K}$ in normal metal N_B. Our model is scale-invariant with respect to the pillar diameter, so we cannot explain the enhanced effective Peltier cooling experimentally found in the narrowest pillars in terms of an intrinsic size effect. However, smaller structures can be more susceptible to the effects of, e.g., incomplete removal of resistive material used during nanofabrication. As discussed above, such extrinsic effects affect the thermoelectric properties and can be treated in our model. The interfacial thermopower $S_{CMS|Au}$ and its spin polarization P_S are basically unknown parameters that may

TABLE III. Interfacial thermoelectric parameters of the F|N|N_B nanopillars at 300 K:[41] Interface Kapitza thermal conductances G_{TH} (W/m^{2}K) (Refs. 42–44) including the phonon contribution (due to the lack of data, the first interface is assumed not to be as thermally conductive as the second interface, for the materials of this table), S (μV/K) is the interfacial Seebeck coefficient, $A_c R$ (fΩm^2) (Refs. 25 and 26) is the cross sectional area times the interface electrical resistance, and P is the spin polarization of the interface conductance.

Material	G_{TH}	S	P	$A_c R$	$\partial R/\partial T$[15,30,33]
CMS|Au	1.8×10^8	−4	0.77	0.915	$\frac{\partial (R_F + R_N)}{\partial T}\Big/2$
Au|Cu	5.9×10^9	3.5	0	0.34	$\frac{\partial (R_N + R_{N_B})}{\partial T}\Big/2$

contribute importantly to the cooling effect in nanostructures, as reflected in the enhancement of the global effective Peltier coefficient $\Pi = 11.2\,\text{mV}$ for $S_1 = -4\,\mu\text{V/K}$ to 23.2 mV for $S_1 = S_{CMS|Au} = -30\,\mu\text{V/K}$; this case is especially relevant in the presence of a resistive N|N_B interface.

The effects of an enhanced interface resistance $A_c R_{1(2)}$ on the Peltier cooling can be tested by varying them between that of a good intermetallic junction to a value corresponding to a thin tunnel barrier. The interface resistance turns out to improve Π as long as the additional Joule heating does not dominate, as illustrated in Fig. 5, since the interface resistance hinders the flow of heat current from the heat baths towards the cooling interface. For parameters from Tables II and III and the non-local interface Joule heating, the total Peltier coefficient reaches a value of $\Pi_{CMS|Au|Cu} = 11.2\,\text{mV}$, close to the experimental result for wider pillars. The temperature profile is plotted in Fig. 7 when the Joule heating is generated locally at the interfaces with 100-fold increased heat and charge resistance and local interface Joule heating, but otherwise the parameters of Fig. 5. The deteriorated cooling performance can be explained by the increased importance of the Joule heating. A linear dependence of the Peltier coefficient was found when varying $A_c R_1$ from 0.915, 9.15, and 91.5 (fΩm^2), resulting in Peltier coefficients $\Pi_{\text{CMS|Au|Cu}}$ of 11.2, 13.49, and 31.61 mV, respectively. For comparison, when the interfaces the Joule heating would be non-local, i.e., $\lambda_A^{ep} + \lambda_B^{ep} = \infty$, the Peltier coefficients increase to 11.28, 14, and 42 mV for the same interface resistances.

Since our calculations take the spin degree of freedom into account, the spin accumulations and spin currents along the nanopillar are by-products of the calculations. In contrast to $|P_F| < 1$, the spin polarization of the derivative of the conductivity $-\infty < P'_F < \infty$. When $P_F < P'_F$, the spin contribution to the cooling power is proportional to the spin accumulations as expressed in Eqs. (36) and (37). A Peltier coefficient of Π of 11.2 mV with parameters from Tables II and III increases by a factor of 2 when $P'_F = -20$. However, if $P'_F > P_F$, the spin degree actually generates heating thereby reducing the cooling power.

We also studied the dependence of the effective cooling on the layer thicknesses L_F, L, and L_B. The Joule heating dominates for a critical current bias I_c that decreases by enlarging L_F. When the thickness of F = CMS is reduced from 40 nm to approximately 5 nm, Π improves slightly from 11.2 to 12.5 mV. The optimal thickness of the ferromagnetic film is $L_F \sim \lambda_F$. The normal metals do not significantly contribute to the cooling, since their Peltier coefficients are relatively small.

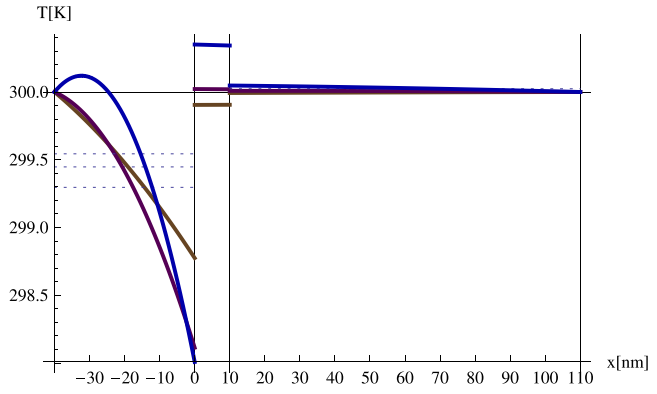

FIG. 7. Temperature distribution in the presence of a dirty N|N_B interface with 10 times the electric ($A_c R_2 = 3.4\,\text{fΩm}^2$) and heat resistances at. $T_0 = 300\,\text{K}$ and for the local interface Joule heating model Eq. (38). Parameters are otherwise the same as in Fig. 5.

Finally, a slight enhancements of the Peltier coefficient can be achieved by an external heat current J_q^{ext} as depicted in the left hand side of Fig. 4 induced by a temperature bias over the pillar $T_L \neq T_0$. This effect and the thermoelectric voltage generation by magnetic nanopillars are left for future study.

V. SUMMARY AND CONCLUSIONS

This paper is motivated by the observed enhancement of the cooling power in magnetic pillars when the cross section was reduced to the nanoscale.[15] We develop a realistic spin, charge, and heat diffusion model to investigate the roles of spin-dependent bulk and interface scattering contributions. We analyzed the (apparent) cooling power and the conditions to maximize the effective Peltier effect.

We demonstrate that very thin (Ohmic) tunnel junctions can improve the cooling power of devices as apparent in the shift of $R(I)$ parabolas. On the other hand, the spin degree of freedom that was thought to be essential in CMS materials appears to be less important for conservatively chosen parameters. However, the material dependence of key parameters is basically unknown. The parameter P'_F, i.e., the spin polarization of the spectral asymmetry of the conductance, turns out to play an important role. This parameter may become arbitrarily large when $\partial(\sigma_F^{\uparrow} + \sigma_F^{\downarrow})/\partial E|_{E_F} = 0$ or, for interfaces $\partial(G_F^{\uparrow} + G_F^{\downarrow})/\partial E|_{E_F} = 0$, which does not seem to be an exotic condition and we recommend a systematic search for such materials or material combinations.[45] Our results also indicate that interfacial parameters such as the interface Seebeck coefficients $S_{1(2)}$ play a very significant role in the thermoelectric characteristics of multilayered pillars and may not be disregarded when validating their performance.

While the experiments up to now have been analyzed in a simple model for the compensation current at which heating and cooling effects cancel, we establish a distributed model of currents and temperatures. The computed temperature profiles along the nanopillar establish that the cooling is not homogeneous, but heating and cooling coexist in different locations of the sample. The current-dependent resistance is only a very crude thermometer that is not a reliable measure for a cooling power.

We find that it is possible to selectively cool a ferromagnet by a few degrees simply by a moderate current flow in the right direction. This could be an important design parameter for STT-MRAMs. The writing of a bit of information by a switching event of the free layer in a memory element is accompanied by significant Joule heating by the electric currents as well as Gilbert heating by the dissipated magnetization dynamics. Applying a small bias current after the

reversal magnetization can assist a quick return to the ambient temperature.

Our model is scale invariant with respect to the pillar diameter and does not provide an intrinsic mechanism for the observed size dependence of the Peltier effect. In principle, extrinsic effects should exist. The large fluctuations observed in the experimental results indicate significant disorder in the smallest nanopillars. The problems are caused by the need to break the vacuum during the microfabrication process of multilayered nanopillars, which may lead to the presence of surface contamination on the $N|N_B$ interface. The effect of pollutants is likely to be more serious for smaller pillars. We found indeed that by modelling interface as a thin tunnel junction enhances the apparent Peltier coefficients by suppressing the heat currents flowing into the pillar from the reservoirs. However, the record cooling effects observed for some of the narrowest pillars appear to be beyond the effects that can credibly be modelled, and we cannot exclude the possibility that something more interesting is going on.

Several effects are beyond the present model approach. Size quantization and the Coulomb blockade are not included. These are not expected to be important in metallic structures at room temperature, but could play a role in heterogeneous materials disordered on a nanometer-scale. Due to the efficient screening, we do not expect that the planar approximation breaks down in nominal pillar structures down to nanometer cross-sections, but hypothetical larger scale disorder might of course introduce inhomogeneous current distributions beyond the present model. Just like phonons, magnons, i.e., excitations of the magnetic order parameter, affect the thermoelectric properties. The magnon-drag effect[46] enhances the Seebeck coefficient, for instance. The longitudinal spin Peltier effect[47] discovered for bilayers with magnetic insulators should also exist in metallic structures: the spin accumulation in the normal metal generates a heat current that comes on top of those discussed here. It is not clear, however, how and why these effects would become so strongly enhanced in nanopillars. More experiments on even smaller and more reproducibly fabricated nanopillars, preferably without breaking the vacuum, are necessary in order to provide hints on what is going on.

We conclude that the Peltier effect in magnetic nanopillars with diameters $\gtrsim 100$ nm appears to be well understood, but that the enhanced values for narrower ones are to date only partly explained. In order to employ the large observed effects, more experiments are necessary in order to shed light on the underlying physical mechanisms.

ACKNOWLEDGMENTS

I.J.A. is grateful to O. Tretiakov, T. Chiba, and A. Cahaya for their fruitful discussions and all members of the Bauer Laboratory at the IMR, Tohoku University, for their hospitality. This work was supported by the National Council for Science and Technology (CONACyT) CVU No. 338381, Mexico-Conacyt CB2015-01 Grant No. 251141 and Instituto Politecnico Nacional (SIP-20160678), JSPS Grants-in-Aid for Scientific Research (KAKENHI) Nos. 25247056, 25220910, and 26103006, FOM (Stichting voor Fundamenteel Onderzoek der Materie), the ICC-IMR, and DFG Priority Programme 1538 "Spin-Caloric Transport" (BA 2954/2).

[1]G. J. Snyder, J.-P. Fleurial, and T. Caillat, J. Appl. Phys. **92**, 1564 (2002).
[2]S. B. Riffat and X. Ma, Appl. Therm. Eng. **23**, 913–935 (2003).
[3]A. J. Minnich, M. S. Dresselhaus, Z. F. Ren, and G. Chen, Energy Environ. Sci. **2**, 466–479 (2009).
[4]M. Johnson and R. H. Silsbee, Phys. Rev. B **35**, 4959 (1987).
[5]M. Hatami, G. E. W. Bauer, Q. Zhang, and P. J. Kelly, Phys. Rev. B **79**, 174426 (2009).
[6]A. Slachter, F. L. Bakker, J.-P. Adam, and B. J. van Wees, Nat. Phys. **6**, 879–882 (2010).
[7]J. Flipse, F. L. Bakker, A. Slachter, F. K. Dejene, and B. J. van Wees, Nat. Nanotechnol. **7**, 166–168 (2012).
[8]G. E. W. Bauer, E. Saitoh, and B. J. van Wees, Nat. Mater. **11**, 391–399 (2012).
[9]A. D. Kent and D. C. Worledge, Nat. Nanotechnol. **10**, 187 (2015).
[10]A. Fukushima, H. Kubota, A. Yamamoto, Y. Suzuki, and S. Yuasa, IEEE Trans. Magn. **41**, 2571 (2005).
[11]L. Gravier, A. Fukushima, H. Kubota, A. Yamamoto, and S. Yuasa, J. Phys. D: Appl. Phys. **39**, 5267 (2006).
[12]A. Sugihara, M. Kodzuka, K. Yakushiji, H. Kubota, S. Yuasa, A. Yamamoto, K. Ando, K. Takanashi, T. Ohkubo, K. Hono, and A. Fukushima, Appl. Phys. Express **3**, 065204 (2010).
[13]H. Katayama-Yoshida, T. Fukushima, V. A. Dinh, and K. Sato, Jpn. J. Appl. Phys., Part 2 **46**, L777 (2007).
[14]N. D. Vu, K. Sato, and H. K. Yoshida, Appl. Phys. Express **4**, 015203 (2011).
[15]S. Bosu, Y. Sakuraba, T. Kubota, I. Juarez-Acosta, T. Sugiyama, K. Saito, M. A. Olivares-Robles, S. Takahashi, G. E. W. Bauer, and K. Takanashi, Appl. Phys. Express **8**, 083002 (2015).
[16]T. Valet and A. Fert, Phys. Rev. B **48**, 7099 (1993).
[17]A. Brataas, G. E. W. Bauer, and P. J. Kelly, Phys. Rep. **427**, 157–255 (2006).
[18]P. C. van Son, H. van Kempen, and P. Wyder, Phys. Rev. Lett. **58**, 2271 (1987).
[19]J. Bass, e-print arXiv:1305.3848.
[20]M. Hatami, G. E. W. Bauer, S. Takahashi, and S. Maekawa, Solid State Commun. **150**, 480–484 (2010).
[21]S. Takahashi and S. Maekawa, Sci. Technol. Adv. Mater. **9**, 014105 (2008).
[22]S. Takahashi and S. Maekawa, J. Phys. Soc. Jpn. **77**, 031009 (2008).
[23]T. M. Nakatani, T. Furubayashi, S. Kasai, H. Sukegawa, Y. K. Takahashi, S. Mitani, and K. Hono, Appl. Phys. Lett. **96**, 212501 (2010).
[24]Y. Sakuraba, K. Izumi, T. Iwase, S. Bosu, K. Saito, K. Takanashi, Y. Miura, K. Futatsukawa, K. Abe, and M. Shirai, Phys. Rev. B **82**, 094444 (2010).
[25]L. L. Henry, Q. Yang, W.-C. Chiang, P. Holody, R. Loloee, W. P. Pratt, Jr., and J. Bass, Phys. Rev. B **54**, 12336 (1996).
[26]Y. Miura, K. Futatsukawa, S. Nakajima, K. Abe, and M. Shirai, Phys. Rev. B **84**, 134432 (2011).
[27]T. Iwase, Y. Sakuraba, S. Bosu, K. Saito, S. Mitani, and K. Takanashi, Appl. Phys. Express **2**, 063003 (2009).
[28]A. Fert, J.-M. George, H. Jaffres, and G. Faini, J. Phys. D: Appl. Phys. **35**, 2443–2447 (2002).
[29]O. Boulle, V. Cros, J. Grollier, L. G. Pereira, C. Deranlat, F. Petroff, G. Faini, J. Barnas, and A. Fert, Nat. Phys. **3**, 492–497 (2007).
[30]Y. Nishi, A. Igarashi, and K. Mikagi, J. Mater. Sci. Lett. **6**, 87–88 (1987).
[31]J.-H. Ku, J. Chang, H. Kim, and J. Eom, Appl. Phys. Lett. **88**, 172510 (2006).
[32]S. Yakata, Y. Ando, T. Miyazaki, and S. Mizukami, Jpn. J. Appl. Phys. **45**, 3892 (2006).
[33]W. Steinhogl, G. Schindler, G. Steinlesber, and M. Engelhardt, Phys. Rev. B **66**, 075414 (2002).
[34]T. M. Tritt, *Thermal Conductivity: Theory, Properties and Applications* (Kluwer Academic/Plenum Publishers, 2004).
[35]F. K. Dejene, J. Flipse, G. E. W. Bauer, and B. J. van Wees, Nat. Phys. **9**, 636 (2013).
[36]H. B. Callen, Phys. Rev. **73**, 1349 (1948).
[37]A. A. Tulapurkar and Y. Suzuki, Phys. Rev. B **83**, 012401 (2011).
[38]R. H. M. Groeneveld and R. Sprik, Phys. Rev. B **51**, 11433 (1995).

[39]R. Khare, P. Keblinski, and A. Yethiraj, Int. J. Heat Mass Transfer **49**, 3401–3407 (2006).
[40]R. Yang, G. Cheng, and M. S. Dresselhaus, Phys. Rev. B **72**, 125418 (2005).
[41]M. Hatami, G. E. W. Bauer, Q. Zhang, and P. J. Kelly, Phys. Rev. Lett. **99**, 066603 (2007).
[42]B. C. Gundrum, D. G. Cahill, and R. S. Averback, Phys. Rev. B **72**, 245426 (2005).
[43]R. M. Costescu, M. A. Wall, and D. G. Cahill, Phys. Rev. B **67**, 054302 (2003).
[44]H. Lyeo and D. G. Cahill, Phys. Rev. B **73**, 144301 (2006).
[45]S. Hu, H. Itoh, and T. Kimura, NPG Asia Mater. **6**, e127 (2014).
[46]M. V. Costache, G. Bridoux, I. Neumann, and S. O. Valenzuela, Nat. Mater. **11**, 199 (2012).
[47]J. Flipse, F. K. Dejene, D. Wagenaar, G. E. W. Bauer, J. Ben Youssef, and B. J. van Wees, Phys. Rev. Lett. **113**, 027601 (2014).